SAND2016-7856C

Calorimetry and Atomic Oxygen Laser-Induced Fluorescence of Pulsed Nanosecond Discharges at Above-Atmospheric Pressures*

Benjamin Wolk and Isaac Ekoto

Combustion Research Facility, Sandia National Laboratories, Livermore, CA, 94551 USA

Abstract. The conversion efficiency of secondary electrical energy into thermal energy was measured in air using an optically accessible spark calorimeter for high-voltage (28 kV peak) pulsed nanosecond discharges with secondary streamer breakdown (SSB) and similar low-temperature plasmas (LTP) without. Initial pressures were varied between 1 and 5 bar absolute, with the anode/cathode gap distances likewise varied between 1 and 5 mm. Secondary electrical energy was measured using an in-line attenuator, with the thermal energy determined from heat-loss corrected pressure-rise calorimetry measurements. The SSB probability at each initial pressure and gap distance was also recorded. The calorimetry measurements confirm that, similar to inductive spark discharges, SSB discharges promote ignition by increasing the local gas temperature. LTP discharges, on the other hand, had very little local gas heating, with electrical-to-thermal conversion efficiencies of ~1%. Instead, the LTP was found to generate substantial O-atom populations — measured using two-photon laser-induced fluorescence near the anode where electric field strengths were strongest — that persisted for 100's of microseconds after the discharge. The influence of 10 repetitive pulses spaced 100 μs apart was also evaluated for a fixed 5 mm electrode gap distance, with the conditional SSB probability for each pulse evaluated using an available photodiode, with the SSB probability found to have increased for each successive pulse. The influence of chemical and thermal preconditioning by the preceding LTP pulse was evaluated, with the increase in SSB occurrence attributed predominantly to mild gas heating that decreased number densities between the electrode gap and hence the gas resistance for the subsequent pulse.

Keywords: Spark Calorimetry, Pulsed Nanosecond Discharge, Low-Temperature Plasma, Atomic Oxygen Two-Photon Laser Induced Fluorescence

1 Introduction

Plasmas — defined here as globally neutral gaseous mixtures of positively- and negatively-charged particles that interact by electric forces in a collective manner — have long been used to control ignition and combustion processes. Conventional inductive

---

* Corresponding Author: Benjamin Wolk (bmwolk@sandia.gov)

coil sparks that feature thermal plasmas with electron energies in equilibrium with the bulk gas energy have fallen out of favor for next-generation automotive engines due to excessive electrode erosion rates from high-temperature arc discharges and poor tolerance to dilution by air or exhaust-gas recirculation (EGR) [1]. Conversely, ignition induced by low-temperature plasma (LTP), where an imbalance exists between ion and electron temperatures, leads to enhanced reaction kinetics as a result of elevated electron energies without the associated translational gas temperature increases that cause electrode erosion. Automotive low-temperature plasma-assisted ignition (PAI) systems extend dilution tolerance limits through the formation of active radicals that shorten ignition delays [2] and rapid heating via electron energy transfer processes [3-5]. Ignition kernel expansion speeds may also be influenced by hydrodynamic instabilities and ionic winds [6, 7]. LTP generated atomic oxygen (O-atom) in particular has been identified as an important radical species that accelerates hydrogen abstraction from the fuel, which in turn increases overall mixture reactivity [8]. For automotive engine combustion, these attributes reduce ignition delay times, suppress knock inducing end-gas auto-ignition, alter fuel reactivity and diffusivity characteristics, and improve noxious emission oxidation [9].

LTP are generally classified by the reduced electric field strength, or the electric field strength (E) normalized by the gas number density (N). Broadly speaking, PAI systems sorted by increasing E/N include: microwaves [3, 10-12], high-frequency resonant discharges [7, 13-16], and pulsed nanosecond discharges (PND) [2, 4, 17-20]. Since LTP related ionization and dissociation rates increase with higher E/N due to limited collisional electron energy transfer effects [21], several recent PAI experiments have focused on PND systems. These igniters typically have E/N greater than 100 Townsend (Td) and electron temperatures above 10 electron volts (eV), while pulse energies remain modest (10s of mJ) due to the truncated discharge [22-25]. Note that secondary streamer breakdown (SSB), where the inter-electrode gas becomes highly electrically conductive, can occur if the gas resistance is sufficiently low (i.e., from low pressures, high temperatures, short electrode gap distances, or gases with low ionization potential) [26, 27]. As a result, the discharge more closely resembles a thermal plasma spark with 2 key differences: (1) the electrical-to-thermal energy transfer is generally more efficient [1, 28], and (2) electrode wear greatly increases due the elevated discharge current.

While electrode erosion issues can be mitigated through the use of dielectric electrode insulators that repel the discharge current [29, 30], the electric field strength becomes compromised with an associated decrease in radical formation rates. Instead it may be preferable to generate LTP without the use of dielectrics, with SSB instead inhibited through the selection of appropriate electrode geometry and pulse discharge characteristics. It is important to note that at engine-relevant pressures, LTP streamer propagation deviates from the well-established self-similar laws (i.e., increased streamer branching, thinner leader structures, and slower than expected streamer velocities) with unknown impact on discharge kinetics [31-33]. Potential causes for the scaling deviation at high-pressure include a change in electron recombination physics [31], less effective streamer cooling by thermal conductivity [34], and photoionization by excited-state nitrogen relaxation [32].

Previous studies have investigated the use of multi-pulse operation, where close-coupled PND with pulse dwell times of ~100 μs are used to continuously augment radical production while ideally avoiding SSB [22, 23]. However, direct discharge imaging during stable engine operation revealed that SSB almost always occurred at some point during the pulse burst; an example image of the luminous SSB event from a 10-pulse burst from Sjöberg et al. [23] is shown in Figure 1. Moreover, once SSB occurs during the burst, each successive discharge in the pulse-burst exhibits SSB biased towards the same cathode site as the first SSB event. The results suggest some sort of ambient gas preconditioning between the electrodes has occurred. Whether the preconditioning mechanism is chemical or thermal remains an open question.

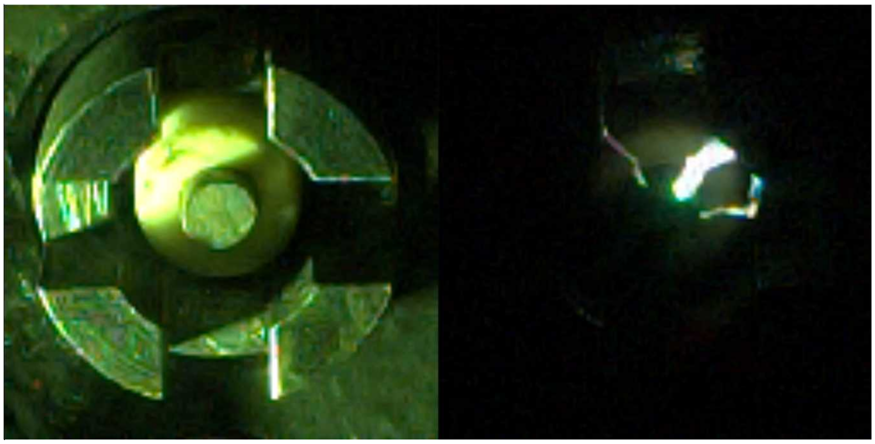

Fig. 1. Image of a 4-prong PND plug in a single-cylinder research engine along with imaging for 10-pulse PND bursts with a 100 μs dwell between successive pulses. Intense luminosity between the central anode and one of four separated cathode sites is indicative of SSB.

The current paper describes experiments performed in a custom-built, optically accessible spark calorimeter used to evaluate high-voltage PND. For all experiments, the test gas was ultra-air with a point-to-point electrode configuration selected so that the local E/N, and hence active radical formation, was maximized near the anode and cathode. Pressure-rise calorimetry was used to measure the electrical-to-thermal energy conversion efficiency for single PND discharges as a function of ambient pressure and electrode gap distance. Calorimetry results were further used to determine the SSB probability for each pressure and gap distance; the electric-to-thermal efficiency was conditionally averaged based on whether the PND remained an LTP or transitioned to a SSB discharge. The SSB probability as a function of initial pressure was further determined for a 10-pulse burst with a fixed 5.0 mm electrode gap distance. Post-discharge *in situ* O-atom populations were also directly measured via two-photon absorption laser induced fluorescence (TALIF) [35, 36] for select LTP-only conditions. Finally, the calorimetry results are used to evaluate potential thermal and chemical mechanisms believed to be responsible for SSB.

2 Experiment Description

All experiments were performed in a custom-built, optically accessible, spark calorimeter illustrated in Figure 2. The calorimeter body is constructed of 316 stainless steel, with a cylindrical 28 cm^3 internal chamber volume ($\mathcal{V}_{cal}$). An inlet port is used to fill ultra-air into the chamber up to the desired pressure (up to 10 bar absolute), with an embedded type-K thermal couple used to measure the initial gas temperature prior to ignition. The calorimeter body also features viewing access of the discharge event through an optical port on the front side wall along with input and output laser access ports that facilitate acquisition of laser-based spectroscopy measurements.

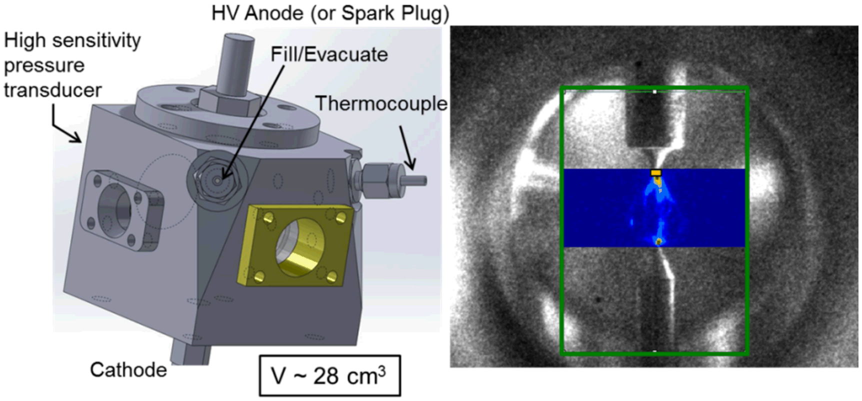

Fig. 2. Illustration of the optically accessible spark calorimeter (left) and an image of the spark gap as visualized through the optical viewing port (right). An image of filtered natural luminosity from the discharge has been superimposed between the electrodes. The TALIF interrogation region is indicated by the orange rectangle near the anode.

2.1 Pressure-Rise Calorimetry

To generate the PND within the spark calorimeter, a Transient Plasma Systems Inc. SSPG-101-HF high-voltage (28 kV peak) pulse generator with a 12 ns full width at half max (FWHM) pulse with and a 5 ns rise time was used. An inline attenuator was used to monitor pulse voltage and current for each discharge event. The high-voltage anode used a modified NGK DP7EA-9 size M12 non-resistive sparkplug that was centrally positioned on the calorimeter top. The anode tip was machined to a rounded point so that local electric field strengths were maximized, while maintaining relatively repeatable discharge characteristics. The plug J-hook and the top 1 cm of material from the outer body ground was removed, with the cathode replaced by a sharpened 3.18 mm diameter steel rod installed from the calorimeter base and secured in place by a Swagelok fitting. Multiple rod lengths were fabricated so that the inter-electrode distance between the anode and cathode could be varied between 1.0 and 5.0 mm. Key calorimeter specifications and operating conditions are summarized in Table 1.

Table 1. Calorimeter specifications and operating conditions.

Calorimeter Internal Volume [cm^3]	28.0
Purge and fill cycle time [s]	90
Initial Temperature [K]	294 ± 5
Initial Pressures [bar]	1.08 – 5.0
Inter-Electrode Distance [mm]	1.0, 2.1, 2.9, 4.0, 5.0

Initial chamber pressures were varied between 1 and 5 bar absolute with initial temperatures fixed at ~294 K. For these conditions, the chamber gas number densities are equivalent to in-cylinder engine conditions with pressures ~3 times greater due to compressive heating. At each gap distance and initial pressure, 30 calorimetry runs were performed. To ensure that residual discharge products did not persist between runs and possibly influence the subsequent spark, chamber contents after each run were purged using fill and vacuum solenoid valves connected to the ultra-air supply and an available vacuum turbo-pump, respectively. Chamber fill pressure was accurately controlled using a Proportion-Air pressure control valve. Differential chamber pressures were measured using a PCB 106B52 high-sensitivity pressure transducer (725 µV/Pa) for initial pressures up to 4 bar and a PCB 106B51 high-sensitivity pressure transducer (145 µV/Pa) for higher initial pressures. Each transducer was secured to the calorimeter using the same Kistler 5134B coupler. All data were recorded using a LeCroy HDO 6054 500 MHz high-definition oscilloscope. Recorded pressures were filtered by a 400 Hz low-pass filter during post-processing. The SSB probability at each initial pressure and gap distance was determined from the resultant pressure record for the single-pulse experiments. The influence of repetitive discharges (up to 10) spaced 100 µs apart were also evaluated for a fixed 5.0 mm electrode gap at pressures up to 2.0 bar. The conditional breakdown probability for each discharge event in the pulse-burst was determined from light emission recorded by a Thorlabs DET210 high-speed photodiode placed an available window port.

Electrical-to-thermal conversion efficiency — defined here as the thermal energy deposited into the gas (E_{therm}) and normalized by the secondary electrical energy delivered (E_{elec}) to the igniter — was determined for each discharge. Secondary electrical energy was obtained by direct integration of the instantaneous electrical power (W), calculated from the product of the inline attenuator voltage (V) and current (I) measurements over the length of each pulse (t_p):

$$E_{elec} = \int_0^{t_p} W(t)dt = \int_0^{t_p} V(t)I(t)dt \tag{1}$$

Gas thermal energy deposition was determined from the volumetric integration of the change in internal energy (δu):

$$E_{therm} = \int \delta u d\mathcal{V} = \int c_v \Delta T d\mathcal{V} = \left(\frac{c_v}{R}\right) \mathcal{V}_{cal} \Delta P = \frac{\mathcal{V}_{cal}\Delta P}{\gamma - 1} \tag{2}$$

where R, c_v, and γ respectively are the gas constant, volumetric heat capacity, and specific heat ratio for air. The pressure-rise (ΔP) was the highest recorded differential pressure measurement from the calorimetry experiments. Due to the small pressure-rises encountered in the experiments, a constant $\gamma = 1.4$ was assumed.

2.2 O-Atom Two-Photon Laser Induced Fluorescence

O-atom TALIF measurements within the spark calorimeter were enabled by 16 mm diameter entrance and outlet laser windows with a 12.9 mm clear aperture that were installed on opposing calorimeter sidewall ports. A larger viewing widow with a 20 mm clear aperture was placed on the sidewall orthogonal to the laser windows. Calorimeter window ports included a 45° beveled seat and copper gasket that mated with a complementary bevel on the front window surface to minimize mechanical stresses that could induce window fracture when the calorimeter was pressurized. A metal retainer was used to secure the windows into the calorimeter via 4 screw holes that mated with tapped holes around the window ports; another copper gasket was placed between the retainer and the window back surface to again minimize mechanical stresses. Two Kalrez O-rings were placed into machined O-ring groves during window installation to eliminate spurious leakage when the calorimeter was pressurized.

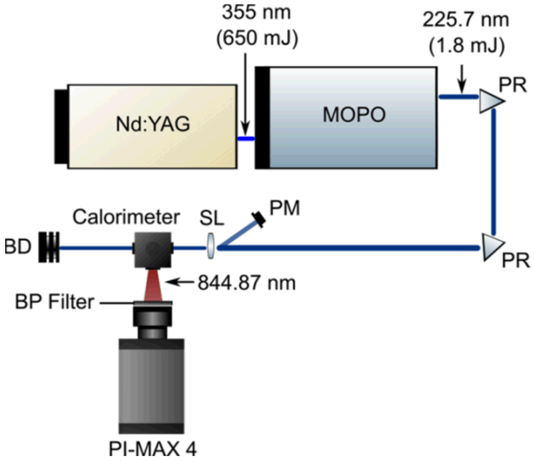

Fig. 3. Diagram of the O-atom TALIF imaging setup into the calorimeter.

O-atom TALIF was excited by a deep-UV laser beam with a 12 ns FWHM pulse width that was generated by an optical parametric oscillator (Spectra-Physics MOPO SL) pumped by an injection-seeded Nd-YAG laser (Spectra-Physics Pro-270); a schematic of the setup is provided in Figure 3. An integrated frequency doubler tuned to 225.7 nm generated the deep UV probe beam. A single plano-convex spherical lens ($f = 100\ mm$) was used to focus the input laser beam just below the spark anode, with the beam diameter ~500 µm at the interrogation region. Laser energy delivered into the spark calorimeter was 1.2-2.5 mJ per pulse, and was monitored using a back reflection off of the spherical lens by a Coherent J-25MB-LE shot resolved laser energy meter. For each operating condition, 50 TALIF images were recorded through the viewing port window via a Princeton instruments PI-MAX 4: 1024 EM intensified camera with a 1024×1024 pixel imaging array. The camera intensifier gate time set to 300 ns. To prevent intensifier damage, only consistent LTP conditions (i.e., SSB probability equals zero) were imaged. A single narrow band filter centered at 850 nm (50 nm FWHM) was used to isolate the $3\,p^3P \rightarrow 3\,s^3S$ transition located near 844.87 nm. The filter did allow stimulated emission of electronically excited atomic nitrogen and oxygen produced by the discharge to pass through (see Figure 2 for a sample image). Accordingly, the earliest O-atom TALIF measurements were recorded 15 μs after the discharge so that all discharge induced luminosity could subside. The maximum camera gain and 2×2 super-pixel binning were used to amplify the signal-to-noise ratio. Flat field and intensifier nonlinear response corrections were implemented using an integrating sphere and arc lamp [37]. To make the results semi-quantitative, TALIF images were corrected for electronic bias, background illumination, and the square of the laser irradiance (to account for the 2-photon absorption process). True quantitative number densities require a more accurate identification of the laser wavelength, which will be accomplished in future TALIF experiments by direct measure of the fundamental wavelength before the frequency doubler by an integrated wavemeter.

High laser irradiances required for sufficient TALIF signal meant the laser entrance and outlet windows could be susceptible to surface etching and/or drilling, which could limit usable window lifespans and lead to costly downtime while replacements are installed. Several design features were accordingly adopted to extend the window service life and simplify the replacement process. A laser shutter was installed to limit laser strikes on the windows to only those needed for the measurements. Standard UV grade quartz (Corning 7980) windows were used because of their superior tolerance to laser damage. Front and back window surfaces were polished with ¼ wave surfaces and had a specified wedge angle of less than 30 seconds. Finally, care was taken to limit the peak irradiance on all window surfaces below 20 MW/cm^2.

3 Results and Discussion

3.1 Pressure-Rise Calorimetry

Ensemble averaged pressure-rise time histories normalized by the peak recorded pressure-rise are plotted for 60 ms after the discharge in Figure 4 for a fixed 5.0 mm electrode gap with initial pressures between 1.08 and 1.52 bar. Pressure-rise traces were conditionally averaged depending on whether they were from LTP (evidenced by peak pressure-rise values below 12 Pa), or from PND that underwent SSB (indicated by peak pressure-rise values that were 100s of pascals). Heat-loss induced pressure decay rates (A) for both the LTP and SSB discharges were extrapolated to time zero using a logarithmic function (equation 3) fit to the respective normalized pressure-rise time histories between 40 and 60 ms after the discharge:

$$\log\left(\frac{\Delta P}{\Delta P_{max}}\right) = A \cdot time(ms) + \log\left(\frac{\Delta P_0}{\Delta P_{max}}\right) \tag{3}$$

Best fit values for A and the normalized regression pressure at time zero ($\Delta P_0/\Delta P_{max}$) for both the LTP and SSB discharges are included in Figure 4. Decay rates for the LTP and SSB discharges are in good agreement with each other, with similar results observed from the pressure-rise time-histories for the other gap distances.

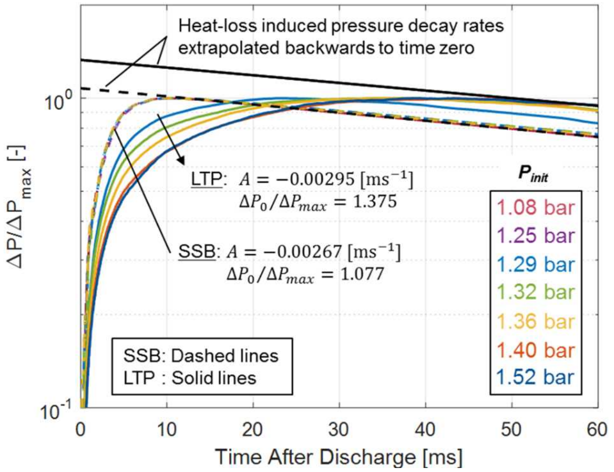

Fig. 4. SSB (dashed) and LTP (solid) post-discharge pressure rise time histories normalized by the peak recorded pressure for a 5.0 mm gap in air for initial pressures between 1.08 and 1.52 bar. Pressure decay rates are also plotted for each discharge.

Normalized SSB discharge pressure-rise time histories collapsed to a common curve, with a single steep pressure-rise that lasted ~8 ms and followed by the heat-loss induced pressure decay. For the LTP discharges, the pressure-rise displayed two distinct stages: (1) a steep initial pressure rise similar to what was observed for the SSB discharges, followed by (2) a shallower, extended pressure rise that lasted another ~20-30 ms. The first stage is believed to result from local gas heating by the discharge and a possible increase in number density due to O_2/N_2 dissociation, while the second stage is believed to be from exothermic recombination of dissociated radicals or electronic state relaxation back to the ground state. The constant pressure decay rates observed 40 ms beyond the discharge suggest that de-excitation of long-lived electronic states such as $O_2(a1)$ was largely complete for all conditions. Unlike the SSB discharges, normalized LTP discharge pressure-rise curves for initial pressures between 1.29 and 1.4 bar did not collapse to a common curve. For these conditions, as the initial pressure increased there was an associated decrease in the proportion of first-stage gas heating. For the two highest evaluated initial pressures (1.4 and 1.52 bar), the traces once again were self-similar, with roughly equal energy deposition into the gas from stages 1 and 2. These results suggest the existence of a LTP-to-SSB transition regime, which will be explored in further detail below.

Single-Pulse SSB Occurrence Probability.

The SSB occurrence probability was determined for a range of electrode gap distances and initial pressures up to 5.0 bar for a single-pulse, with the results plotted in Figure 5. At all gap distances above a threshold initial pressure there was a relatively steep decline in SSB occurrence probability, with the fall-off sharper for larger electrode gap distances. For the 1.0 mm gap, 100% SSB occurrence probabilities were observed for initial pressures below 3 bar, with at least some marginal chance for SSB occurrence at all initial pressures explored in the current study. When the gap distances were increased, the initial pressures where SSB was observed dropped. With the largest 5.0 mm gap, no SSB was observed for initial pressures above 1.4 bar. Note that for the 5.0 mm gap, the 3 initial pressures in the transition regime where inconsistent SSB were observed are the same LTP-to-SSB transition conditions identified from the pressure-rise time histories in Figure 4. These results suggest that complete SSB did not occur for before the discharge was terminated.

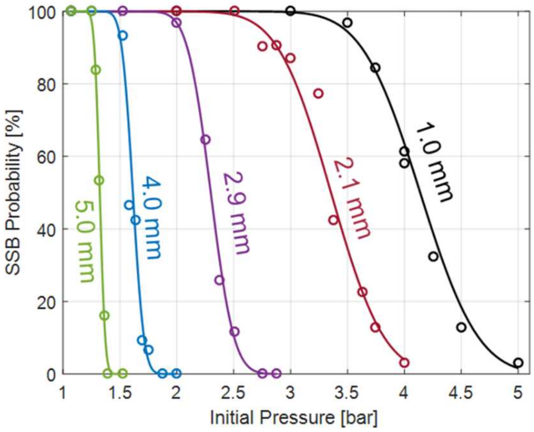

Fig. 5. SSB occurrence probability as a function of initial pressure and gap size for a single 28 kV discharge in air.

Electrical-to-Thermal Energy Conversion Efficiency.

Calculated pulse electric energy (equation 1) for the SSB and LTP discharges from the in-line attenuator discharge voltage and current measurements are plotted in Figure 6a. LTP discharges electrical energy — regardless of the initial pressure, electrode gap distance, or whether it overlapped with the LTP-to-SSB transition regime — was relatively consistent at around 15 mJ. For SSB discharges in the LTP-to-SSB transition regime (highlighted in the dashed rectangle in Figure 6a), the discharge electrical energy more than doubled to around 38 mJ as the significant decrease in inter-electrode gas resistance led to a large jump in current flow between the anode and cathode. For SSB discharges outside of the LTP-to-SSB transition regime, the delivered discharge electrical energy further jumped to around 48 mJ; the exception was for the 1.0 mm gap where the discharge electrical energy remained around 40 mJ.

The electric-to-thermal conversion efficiency was calculated for all LTP and SSB conditions using the discharge electrical energy from equation 1 and the thermal energy deposited in the gas from equation 2, with all results plotted in Figure 6b. When the initial pressure was 1.08 bar, the SSB discharge electric-to-thermal conversion efficiency for the 1.0 mm gap was just over 5%, with this value monotonically increasing to 12% as the initial pressure increased to 5.0 bar. As the gap distances increased, there was a proportional increase in the electrical-to-thermal conversion efficiency for the SSB discharges, with a peak value of 38% observed for the 5.0 mm gap with a 1.25 bar initial pressure. For the larger gap distances, the electrical-to-thermal conversion efficiency likewise increased with initial pressure until the LTP-to-SSB transition region was reached. At this point the efficiency numbers decreased, with the decrease becoming more precipitous for the larger gap distances.

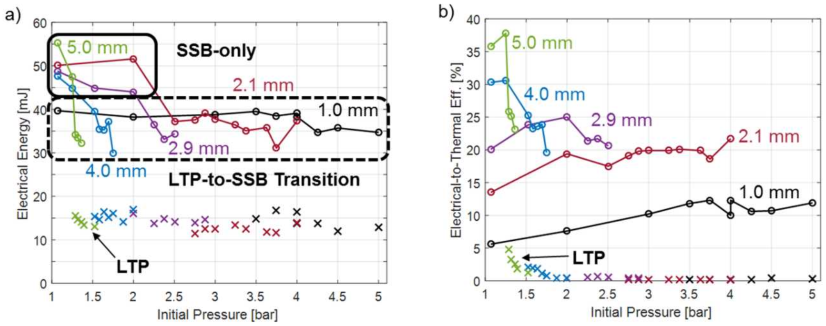

Fig. 6. Plots of (a) electrical energy and (b) electrical-to-thermal energy conversion efficiency for SSB discharges (○) and for LTP discharges without SSB (x) as a function of gap size and initial pressure.

Electrical-to-thermal conversion efficiencies for the LTP discharges were almost uniformly low, with most values below 1% regardless of the initial pressure or gap distance. The exception was for the 5.0 mm gap (and to a lesser extent the 4.0 mm gap), where in the LTP-to-SSB transition regime LTP electrical-to-thermal conversion efficiencies increased to ~5% for the 1.29 bar initial pressure condition. These results confirm that LTP discharges at this condition flirt with a transition to SSB.

Multi-Pulse SSB Occurrence Probability.

The SSB occurrence probability for a 10 pulse burst with a 100 µs dwell between each pulse was evaluated for a fixed 5.0 mm gap at a range of initial pressures up to 2 bar. The first pulse where SSB occurred was identified by whether or not luminous emission was observed by a photodiode positioned at the laser exit window. Note that after the first observance of SSB, SSB was observed in all successive discharge events in the pulse train. Accordingly, only the conditional probability for each pulse is plotted in Figure 7, where discharges preceded by SSB were excluded from the statistics. Note further that the SSB occurrence probability as a function of pressure for the first pulse was nearly identical to the SSB occurrence probability in Figure 5 for the 5.0 mm gap obtained from the pressure-rise calorimetry measurements. The good agreement suggests that (1) the first discharge in the 10-pulse burst was well matched to the single-pulse results, (2) the experiment setup is highly repeatable, and (3) the photodiode is capable of reproducing similar SSB probability results as the calorimetry.

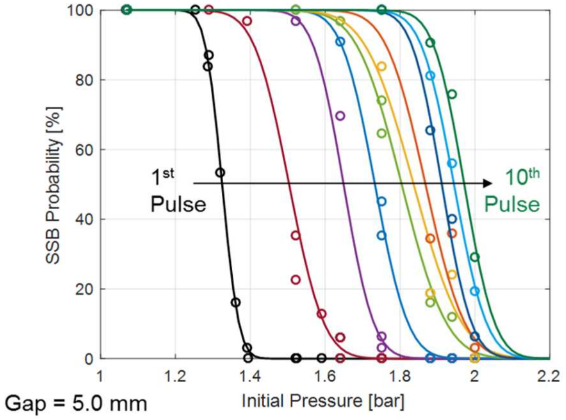

Fig. 7. SSB probability for each pulse in a 10-pulse burst with a 100 μs dwell between successive discharges as a function of initial pressure and with a fixed 5.0 mm electrode gap distance.

If subsequent discharges in the 10-pulse burst had no dependence on gas preconditioning from the previous pulse, then the conditional averaging process should produce identical SSB probability curves as a function of initial pressure. However, from Figure 7 this is not the case with each successive pulse resulting in a rightward shift of the SSB probability curve towards higher initial pressures. The highest initial pressure where SSB was observed shifted from 1.25 bar for the first pulse to around 2.1 bar for the tenth pulse. The magnitude of the shift lessened with each successive pulse, with data from the 10th pulse nearing an asymptote. The results demonstrate that with close-coupled multi-pulse discharges, SSB can occur at conditions where there otherwise would have been no chance for SSB occurrence due to some form of thermal or chemical preconditioning from previous pulses.

To more clearly illustrate the discharge characteristics for multi-pulse operation in the LTP-to-SSB transition regime, a scatter plot of the delivered pulse electrical energy for the first 5 pulses of each test when the initial pressure was 1.6 bar is provided in Figure 8a. Respective regions where the discharges were clearly LTP (i.e., less than 20 mJ delivered electric energy) or SSB (i.e., greater than 35 mJ delivered electric energy) are labeled. Pulses in between the dashed lines are believed to be from the LTP-to-SSB transition discharges.

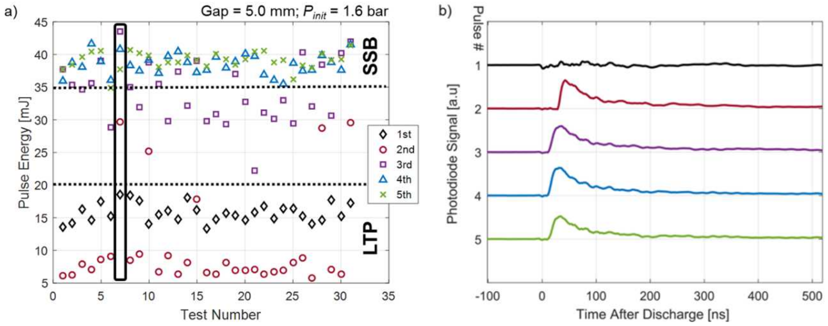

Fig. 8. (a) Discharge electrical energy for the first 5 pulses in the 10-pulse burst; LTP and SSB regions are identified by the dashed lines. (b) The photodiode signal time history for each pulse in Test Number 7, highlighted in Figure 8a.

For the test sequence in Figure 8a, each first pulse in the burst was LTP with all delivered pulse electric energies around 15 mJ. In most instances the second pulse likewise remained LTP, although the pulse energy roughly halved to around 8 mJ. There were 4 recorded instances where the second pulse transitioned into the LTP-to-SSB regime. By the third pulse, all discharges had delivered pulse energies that were characteristic of the LTP-to-SSB transition regime or were full SSB discharges. For all subsequent pulses, the discharges were firmly in the SSB regime.

In Figure 8b, the photodiode time-history for each pulse from Test 7 in the sequence (highlighted in Figure 8a) is shown for each discharge event. Based on the delivered pulse energies for this test, the first pulse was LTP, with the second pulse in the LTP-to-SSB transition region and all subsequent pulses in the SSB regime. As expected, there was very little luminosity from the LTP of the first pulse. For each subsequent pulse, there was a rapid rise in photodiode signal shortly after the discharge indicative of SSB; the peak recorded photodiode signal is relatively consistent for each discharge. However, intense luminosity was not detected by the photodiode until ~30 ns after the discharge for the second pulse, which roughly doubled the ~15 ns dwell time observed for all subsequent SSB pulses. The delayed luminosity is a clear indication that a delay in the onset of SSB is related to the characteristic LTP-to-SSB discharges observed for the second pulse.

In Figure 9, discharge power, current, and voltage traces for Pulse 2 (LTP-to-SSB discharge) and Pulse 3 (SSB discharge) from Test Number 7 in Figure 8a are overlaid with the corresponding photodiode signal from Figure 8b. For both pulses, the voltage initially experienced a rapid rise (~5 ns) shortly after the discharge as the primary streamer head advanced toward the cathode. Free electrons generated by the ionization processes within the streamer flooded back toward the anode, leading to a large increase in discharge current (~125 amps) and a rapid rise in voltage potential rise (~20 kV). Once the primary streamer connected to the cathode, there was a rapid drop in voltage potential as a negative charge "return wave" flooded the primary streamer channel with electrons from the cathode. The discharge current likewise experienced a rapid decline. For both pulses, most discharge energy was delivered during this primary streamer process.

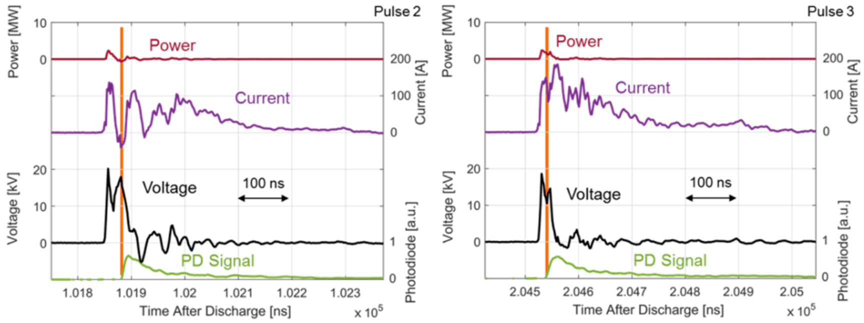

Fig. 9. Power, current, voltage, and photodiode time-history traces for Pulses 2 and 3 from Test Number 7 in Figure 8a.

Concurrent with the rapid primary streamer advance and attachment to the cathode was the slower secondary streamer propagation also from the anode to the cathode, with the propagation speeds dictated by the local electric field strength. A second voltage spike that resulted from secondary streamer ionization processes is observed in the respective voltage time histories, with peak values roughly 20 – 30 ns after the discharge. For both Pulse 2 and Pulse 3, the peak voltage from the secondary streamer induced voltage spike closely corresponded with the appearance of photodiode luminosity indicative of SSB (highlighted by the orange vertical line in both plots).

The central difference between the two discharge events is the apparent slower secondary streamer propagation speeds for Pulse 2, which meant the primary streamer current was effectively zero by the time the secondary streamer connected with the cathode. While the current subsequently increased sharply due to the decrease in gas resistance between the electrodes, there was a commensurate drop in voltage potential as the supplied electrical pulse had already terminated. The net result was that there was very little delivered electrical energy after the SSB event. Pulse 3 on the other hand, exhibited a secondary streamer voltage spike with a sharper rise rate that is indicative of faster secondary streamer propagation velocities. As a result, the secondary streamer was able to connect to the cathode while the overall gap current remained relatively high. The combination of elevated voltage and current values that coincided with the SSB discharge led to an associated increase in delivered electrical energy into the electrical gap.

3.2 LTP Two-Photon Laser Induced Fluorescence

O-atom TALIF was performed in the optically accessible calorimeter for the 5.0 mm gap with an initial pressure of 1.7 bar. The condition was selected because there was no observance of SSB for either the first or second pulse from the pressure-rise calorimetry experiments. As mentioned in the experiment description section, the laser beam focus was positioned as close to the anode as possible; it was obvious when the beam clipped the anode as luminous bits of metal fluorescence was observed in the TALIF images. The region below the anode was selected because this is where the largest electric field strengths are located ($E/N \approx 536$), and because it was only location where consistent O-atom TALIF was observed. Signal was recorded for 50 consecutive discharges, with purge and fill cycles performed between each discharge as described earlier. O-atom TALIF images were recorded at discrete times after the discharge, beginning at 15 μs post-discharge (selected to avoid discharge induced emission as described earlier) and continuing until 200 μs post-discharge.

A sample image of the ensemble averaged TALIF measurement near the anode is provided in Figure 10. Also included in Figure 10 is a plot of the irradiance corrected TALIF signal intensity as a function of time after the discharge; both single and double-pulsed TALIF signal data are shown. Each data point represents the ensemble average of the 2 super pixels with the highest recorded signal from each frame. Although the data are not quantitative O-atom number densities, they are nonetheless useful to compare relative concentrations as a function of time after the discharge and how a single or double pulse impacts O-atom formation rates.

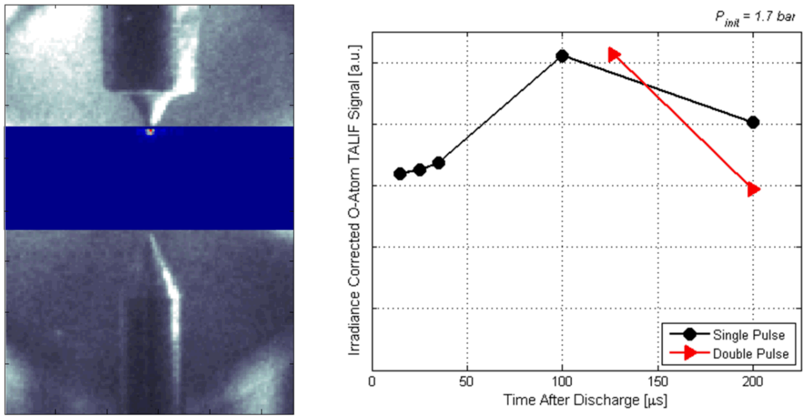

Fig. 10. Point (left) image of O-atom TALIF. Plotted on the right are the irradiance corrected TALIF signal data as a function of time after the discharge for single (black) and double (red) pulse operation.

O-atom TALIF signal increased roughly 60% between 15 and 100 μs after the discharge, with a decline thereafter. These results are consistent with the measured O-atom number densities observed by Pendleton et al. [35] for a similar discharge in ambient air, although they observed a sharp decline in O-atom concentrations by 100 μs after the discharge, with no observable concentrations by 200 μs post-discharge. These results are somewhat surprising since recombination rates for the current setup are expected to be faster with the higher initial pressure. However, it is important to note that the pulse characteristics for the Pendleton et al. study were somewhat different, with a shallower rise-time along with lower peak voltages and currents. It is possible that larger O-atom concentrations at elevated electronic states were created with the current setup, with ground state O-atom populations being continuously fed by the collisional de-excitation of these species. Additional measurements are needed to verify this result.

Double pulse data were also acquired, with the results plotted in Figure 10 referenced to the first of the two pulses. It is interesting that the O-atom populations at 127 and 200 µs after the first pulse are nearly identical to the single-pulse values acquired at the same time after the pulse. Possible reasons for this observation include (1) the second pulse induced some fluid mechanic process that displaced some of ground state O-atom populations generated by the first pulse, (2) ground state O-atom populations were completely saturated due to a lack of available diatomic oxygen, or (3) products created by the second pulse consumed much of the ground state O-atom generated by the preceding pulse. It is also important to note that the first discharge event resulted in some nominal gas heating between the electrodes. As a result, the total number density at the anode during and after the second discharge would likely be lower than for the first condition. Gas heating by the preceding discharge event process will be evaluated in the next section.

3.3 Discussion

It remains unclear why subsequent discharges from multi-pulse operation led to higher SSB probabilities relative to the previous discharge. There are two likely mechanisms that led to some sort of gas preconditioning between the electrodes by the preceding pulse that make the subsequent pulse more sensitive to breakdown. For the first mechanisms, we postulate there is a chemical effect where the preceding LTP pulse discharge leads to the formation of new species (e.g., O-atom, atomic nitrogen, nitrogen oxide, ozone) or excited states that persist well after the original discharge effectively lowered the overall gas ionization potential (IP) for the next discharge. For the second mechanism, we consider the effect of modest gas heating by the preceding LTP discharge, which would reduce the local number density and hence the effective resistance of the gas between the electrodes.

To evaluate the chemical mechanism, the IP of commonly generated LTP species from discharges in air are considered, with the values tabulated in Table 3. Note that the only electronic excited state considered was $O_2(a1)$, which has decay lifetimes on the order of milliseconds in ambient air; all other possible electronic excited states have lifetimes that are no longer than a few nanoseconds. From Table 3, it is notable while N_2 has the highest IP relative to the other species, O_2 is among the lowest with ground state O-atom and ozone (O_3) having IP higher than O_2. Moreover, while the dissociation of N_2 into atomic nitrogen (N) would decrease the IP on a molar basis, the increase in number density would decrease the local reduced electric field. Only substantial production of nitrogen oxide (NO) or electronically excited $O_2(a1)$ would appear to reduce the gap IP in an appreciable way without leading to an associated reduction in E/N. Future experiments will seek to measure NO concentrations between the gap to evaluate via laser-induced fluorescence. It should be noted that chemical modeling simulations using the GRI 3.0 NOx [38] chemistry mechanism indicate that most dissociated N would recombine as N_2 rather than form NO. Moreover, NO equilibrium formation rates are ~1 ms, which is much longer than the 100 µs dwell between successive pulses used for the experiments here. It is thus concluded that while chemical effects are important, they are likely not a major driver for the increased incidence of SSB.

Table 2. Ionization potentials for oxygen, nitrogen, and other LTP generated species.

Species	IP [eV]
O_2	12.1
N_2	15.6
NO	9.3
O_3	12.5
O	13.6
N	14.5
O_2(a1)	11.1

The thermal mechanism was evaluated by making the assumption that all thermal energy measured from the LTP-discharge calorimetry experiments was initially deposited into a cylindrical region that spanned the electrode gap. A uniform temperature increase ($\varDelta T$) in the volume was then estimated as the thermal energy normalized by the total heat capacity of the volume following equation 4.

$$\varDelta T = E_{Therm} / \left(\rho c_p \mathcal{V}_{spark}\right) \tag{4}$$

Here, ρ and c_p are the density and heat capacity at constant pressure for air, while $\mathcal{V}_{spark}$ is the estimated initial cylinder volume of the spark channel. The spark channel diameter was estimated to be 625 µm based on the natural luminosity images acquired during the discharge event.

The initial temperature profile in the radial direction was then imposed as a boundary equation for a one-dimensional heat equation (in cylindrical coordinates), with the surrounding fluid set to the initial temperature prior to the discharge. To eliminate a discontinuity in the boundary condition between the cylinder and the surrounding ambient fluid, the initial profile was specified as an error function. The evolution of the temperature profile was then computed at discrete time intervals using the Matlab Partial Differential Equations tool box. An example profile of the of the initial temperature and the corresponding profile 100 µs later is provided in Figure 11 for the calorimeter test with a 5.0 mm gap and a 1.4 bar initial pressure. For this condition, about 240 µJ of thermal energy was measured from the single-pulse calorimetry experiments, which from equation 4 led to a modest temperature increase in the initial spark volume ($\varDelta T = 93\ K$). By 100 µs after the first discharge the centerline temperature was essentially unchanged, which meant the centerline number density had effectively decreased ~24% between the first and second pulses.

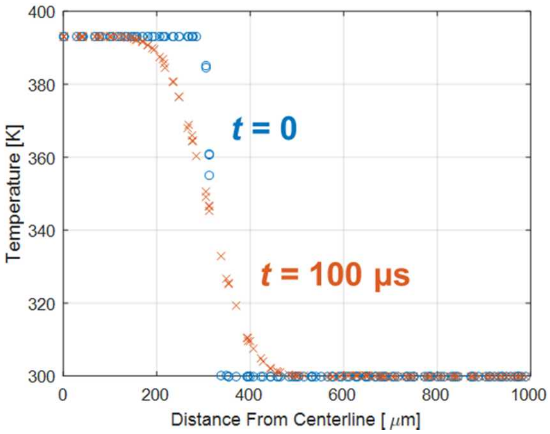

Fig. 11. Calculated temperature profiles at 0 and 100 μs after the discharge for a single-pulse calorimetry experiment with a 1.4 bar initial pressure and a 5.0 mm electrode gap. The initial profile temperature was set from equation 4 assuming that a 625 μm diameter cylinder extended between the electrodes and $E_{therm} = 240\ \mu J$ from the calorimetry experiments.

From Figure 5, he SSB occurrence probability was nearly zero when the initial pressure was 1.4 bar. By the subsequent pulse, the 24% decrease in number density due to the increased temperature would have resulted in an effective decrease in initial pressure for the second pulse to 1.07 bar, which for the single-pulse data would have resulted in 100% SSB occurrence probability. This SSB probability in fact agrees very well with the second pulse data for the 1.4 bar condition. Similar effects were observed for the other conditions. Based on these results, the proposed thermal mechanism appears to be predominantly responsible for the gas preconditioning between successive close coupled PND pulses.

4 Conclusions

The conversion efficiency of delivered electrical energy into thermal energy in air was measured in a spark calorimeter modified for optical viewing and laser access for high-voltage (28 kV peak) PND (5 ns rise time, 12 ns FWHM) that underwent SSB or remained LTP. Initial pressures were varied between 1 and 5 bar, with the gap distances between a sharpened anode and cathode varied between 1 and 5 mm. Secondary electrical energy was measured using an in-line attenuator, while the thermal energy deposited into the gas was determined from the pressure-rise calorimetry measurements. The probability for single-pulse SSB occurrence was evaluated using the calorimetry measurements. The SSB occurrence probability for a 10 pulse burst with a 100 μs dwell between each pulse was also evaluated for a fixed 5.0 mm gap at a range of initial pressures up to 2 bar. Here, SSB was identified by luminous emission recorded by a photodiode positioned at an available laser exit window. Finally, for

LTP-only discharges with either single or double-pulse operation in situ O-atom TALIF was performed near the anode where electric field strengths were strongest. Major findings are as follows:

- The SSB occurrence probability for single-pulse PND decreased with larger gap distances and lower initial pressures. For all gap distances evaluated, SSB-to-LTP transition regions were identified where intermittent SSB would occur.
- Electrical energies for single-pulse LTP were ~15 mJ with less than 1% of the electrical energy converted into thermal energy, except for the 5 mm gap where the thermal energy conversion increased to 5% in the SSB-to-LTP region. SSB from the SSB-to-LTP regime more than doubled (~38 mJ), with up to 25% of the electrical energy converted into thermal heating. SSB outside of the SSB-to-LTP transition region had even higher delivered electrical energies (45 mJ+) and conversion efficiencies (30%+) at the larger gap distances. Differences in SSB behavior were attributed to slower secondary streamer propagation rates for discharges in the SSB-to-LTP regime.
- For close-coupled multi-pulse PND, SSB probabilities were found to increase with each successive pulse. The increased occurrence was attributed mostly a thermal preconditioning mechanism from the preceding LTP pulse, modest heating of the gas between the electrodes lowered the number density and hence the electrical resistance for gases within the electrode gap.
- Significant O-atom populations were measured via TALIF just below the anode beginning ~15 µs after a LTP discharge for an initial pressure of 1.7 bar; the results agreed well with previous measurements from a similar setup, but at atmospheric pressure. Double-pulse operation was found to found to have negligible influence on the post-discharge O-atom populations near the anode. Additional planar O-atom TALIF imaging is needed to determine if the pulse induced advection displaced O generated by the previous pulse.

The results suggest that to maximize active radical formation via LTP when PND are used, dwell times between successive pulses should be long enough to allow for the inter-electrode gas temperatures to relax back to ambient, or that successive pulse energies should be lowered to lessen the possibility of SSB. Moreover strong tumble flows could enable rapid and continuous refreshment of cooler ambient gases provided that the electrode design does not obstruct flows between the anode and cathode.

5 Acknowledgements

This work was performed at the Combustion Research Facility, Sandia National Laboratories, Livermore, CA. Financial support was provided by the U.S. Department of Energy, Office of Vehicle Technologies. Sandia National Laboratories is a multi-program laboratory managed and operated by Sandia Corporation, a wholly owned subsidiary of Lockheed Martin Corporation, for the U.S. Department of Energy's National Nuclear Security Administration under contract DE-AC04-94AL85000. The authors gratefully acknowledge the hardware support and fruitful technical discussions from Daniel Singleton and Jason Sanders of Transient Plasma Systems Inc. We further acknowledge technical engine data provided by Magnus Sjöberg of Sandia National Laboratories along with James Sevik, Riccardo Scarcelli, and Thomas Wallner of Argonne National Laboratory.

6 References

1. Dale JD, Checkel MD, Smy PR, "Application of high energy ignition systems to engines," *Prog Energ Combust*, 23 (5-6):379-98, 1997, doi: 10.1016/S0360-1285(97)00011-7.
2. Sun WT, Uddi M, Won SH, Ombrello T, Carter C, Ju YG, "Kinetic effects of non-equilibrium plasma-assisted methane oxidation on diffusion flame extinction limits," *Combustion and Flame*, 159 (1):221-9, 2012, doi: 10.1016/j.combustflame.2011.07.008.
3. Wolk B, DeFilippo A, Chen JY, Dibble R, Nishiyama A, Ikeda Y, "Enhancement of flame development by microwave-assisted spark ignition in constant volume combustion chamber," *Combustion and Flame*, 160 (7):1225-34, 2013, doi: 10.1016/j.combustflame.2013.02.004.
4. Mintusov E, Serdyuchenko A, Choi I, Lempert WR, Adamovich IV, "Mechanism of plasma assisted oxidation and ignition of ethylene-air flows by a repetitively pulsed nanosecond discharge," *P. Combust. Inst.*, 32:3181-8, 2009, doi: 10.1016/j.proci.2008.05.064.
5. Kosarev IN, Aleksandrov NL, Kindysheva SV, Starikovskaia SM, Starikovskii AY, "Kinetics of ignition of saturated hydrocarbons by nonequilibrium plasma: CH4-containing mixtures," *Combustion and Flame*, 154 (3):569-86, 2008, doi: 10.1016/j.combustflame.2008.03.007.
6. Jaggers HC, von Engel A, "Effect of Electric Fields on Burning Velocity of Various Flames," *Combustion and Flame*, 16 (3):275-&, 1971, doi: 10.1016/S0010-2180(71)80098-6.
7. Leonov SB, Yarantsev DA, "Plasma-induced ignition and plasma-assisted combustion in high-speed flow," *Plasma Sources Sci T*, 16 (1):132-8, 2007, doi: 10.1088/0963-0252/16/1/018.
8. Ju YG, Lefkowitz JK, Reuter CB, Won SH, Yang XL, Yang S, et al., "Plasma Assisted Low Temperature Combustion," *Plasma Chem Plasma P*, 36 (1):85-105, 2016, doi: 10.1007/s11090-015-9657-2.
9. Ju YG, Sun WT, "Plasma assisted combustion: Progress, challenges, and opportunities," *Combustion and Flame*, 162 (3):529-32, 2015, doi: 10.1016/j.combustflame.2015.01.017.
10. Nishiyama A, Ikeda Y, "Improvement of Lean Limit and Fuel Consumption Using Microwave Plasma Ignition Technology," SAE International 2012-01-1139, 2012, doi: 10.4271/2012-01-1139.
11. Wang Q, Zhang G, Liu Y, Hou L, Liu C, Microwave plasma ignition process of methane and air mixture under high pressure. Proc Pulsed Power Conference (PPC), 2013 19th IEEE, 16-21 June 2013, 2013, p. 1-3.
12. Michael JB, Chng TL, Miles RB, "Sustained propagation of ultra-lean methane/air flames with pulsed microwave energy deposition," *Combustion*

and Flame, 160 (4):796-807, 2013, doi: 10.1016/j.combustflame.2012.12.006.

13. Chintala N, Bao AN, Lou GF, Adamovich IV, "Measurements of combustion efficiency in nonequilibrium RF plasma-ignited flows," *Combustion and Flame*, 144 (4):744-56, 2006, doi: 10.1016/j.combustflame.2005.08.040.
14. Pertl FA, Smith JE, "High-Level Modeling of an RF Pulsed Quarter Wave Coaxial Resonator with Potential use as an SI Engine Ignition Source," SAE International 2008-01-0089, 2008, doi: 10.4271/2008-01-0089.
15. Hampe C, Kubach H, Spicher U, Rixecker G, Bohne S, "Investigations of Ignition Processes Using High Frequency Ignition," SAE International 2013-01-1633, 2013, doi: 10.4271/2013-01-1633.
16. Mariani A, Foucher F, Moreau B, "The Effects of a Radio Frequency Ignition System on the Efficiency and the Exhaust Emissions of a Spark-Ignition Engine," SAE International 2013-24-0053, 2013, doi: 10.4271/2013-24-0053.
17. Bozhenkov SA, Starikovskaia SM, Starikovskii AY, "Nanosecond gas discharge ignition of H-2- and CH4- containing mixtures," *Combustion and Flame*, 133 (1-2):133-46, 2003, doi: 10.1016/S0010-2180(02)00564-3.
18. Kosarev IN, Aleksandrov NL, Kindysheva SV, Starikovskaia SM, Starikovskii AY, "Kinetic mechanism of plasma-assisted ignition of hydrocarbons," *J Phys D Appl Phys*, 41 (3) 2008, doi: 10.1088/0022-3727/41/3/032002.
19. Adamovich IV, Choi I, Jiang N, Kim JH, Keshav S, Lempert WR, et al., "Plasma assisted ignition and high-speed flow control: non-thermal and thermal effects," *Plasma Sources Sci T*, 18 (3) 2009, doi: 10.1088/0963-0252/18/3/034018.
20. Won SH, Jiang B, Dievart P, Sohn CH, Ju YG, "Self-sustaining n-heptane cool diffusion flames activated by ozone," *P. Combust. Inst.*, 35:881-8, 2015, doi: 10.1016/j.proci.2014.05.021.
21. Starikovskiy A, Aleksandrov N, "Plasma-assisted ignition and combustion," *Prog Energ Combust*, 39 (1):61-110, 2013, doi: http://dx.doi.org/10.1016/j.pecs.2012.05.003.
22. Sevik J, Wallner T, Pamminger M, Scarcelli R, Singleton D, Sanders J, "Extending Lean and Egr-Dilute Operating Limits of a Modern Gdi Engine Using a Low-Energy Transient Plasma Ignition System," *Proceedings of the Asme Internal Combustion Engine Division Fall Technical Conference, 2015, Vol 1*, 2016.
23. Sjöberg M, Zeng W, Singleton D, Sanders JM, Gundersen MA, "Combined Effects of Multi-Pulse Transient Plasma Ignition and Intake Heating on Lean Limits of Well-Mixed E85 DISI Engine Operation," *SAE Int. J. Engines*, 7 (4):1781-801, 2014, doi: 10.4271/2014-01-2615.
24. Breden D, Raja LL, Idicheria CA, Najt PM, Mahadevan S, "A numerical study of high-pressure non-equilibrium streamers for combustion ignition application," *J Appl Phys*, 114 (8) 2013, doi: 10.1063/1.4818319.

25. Shiraishi T, Urushihara T, Gundersen M, "A trial of ignition innovation of gasoline engine by nanosecond pulsed low temperature plasma ignition," *J Phys D Appl Phys*, 42 (13) 2009, doi: 10.1088/0022-3727/42/13/135208.
26. Bastien F, Marode E, "Breakdown Simulation of Electronegative Gases in Non-Uniform Field," *J Phys D Appl Phys*, 18 (3):377-93, 1985, doi: 10.1088/0022-3727/18/3/007.
27. Ono R, Oda T, "Formation and structure of primary and secondary streamers in positive pulsed corona discharge - effect of oxygen concentration and applied voltage," *J Phys D Appl Phys*, 36 (16):1952-8, 2003, doi: 10.1088/0022-3727/36/16/306.
28. Teets RE, Sell JA, "Calorimetry of Ignition Sparks," SAE International 1988, doi: 10.4271/880204.
29. Gibalov VI, Pietsch GJ, "The development of dielectric barrier discharges in gas gaps and on surfaces," *J Phys D Appl Phys*, 33 (20):2618-36, 2000, doi: 10.1088/0022-3727/33/20/315.
30. Shiraishi T, Urushihara T, "Fundamental Analysis of Combustion Initiation Characteristics of Low Temperature Plasma Ignition for Internal Combustion Gasoline Engine," SAE International 2011-01-0660, 2011, doi: 10.4271/2011-01-0660.
31. Babaeva NY, Naidis GV, "On streamer dynamics in dense media," *J Electrostat*, 53 (2):123-33, 2001, doi: 10.1016/S0304-3886(01)00135-8.
32. Liu N, Pasko VP, "Effects of photoionization on similarity properties of streamers at various pressures in air," *J Phys D Appl Phys*, 39 (2):327-34, 2006, doi: 10.1088/0022-3727/39/2/013.
33. Lin YH, Singleton D, Sanders J, Kuthi A, Gundersen MA, Pressure effects on transient plasma discharge in air. Proc Pulsed Power Conference (PPC), 2013 19th IEEE, 16-21 June 2013, 2013, p. 1-5.
34. Tardiveau P, Marode E, Agneray A, Cheaib M, "Pressure effects on the development of an electric discharge in non-uniform fields," *J Phys D Appl Phys*, 34 (11):1690-6, 2001, doi: 10.1088/0022-3727/34/11/321.
35. Pendleton SJ, Bowman S, Carter C, Gundersen MA, Lempert W, "The production and evolution of atomic oxygen in the afterglow of streamer discharge in atmospheric pressure fuel/air mixtures," *J Phys D Appl Phys*, 46 (30) 2013, doi: 10.1088/0022-3727/46/30/305202.
36. Zhang S, van Gessel AFH, van Grootel SC, Bruggeman PJ, "The effect of collisional quenching of the O 3p P-3(J) state on the determination of the spatial distribution of the atomic oxygen density in an APPJ operating in ambient air by TALIF," *Plasma Sources Sci T*, 23 (2) 2014, doi: 10.1088/0963-0252/23/2/025012.
37. Williams TC, Shaddix CR, "Simultaneous correction of flat field and nonlinearity response of intensified charge-coupled devices," *Rev Sci Instrum*, 78 (12) 2007, doi: 10.1063/1.2821616.
38. GRI-Mech 3.0, The Gas Research Institute. Available from: http://www.me.berkeley.edu/gri_mech/.